



HAL
open science

Assessing the Surface Chemistry of 2D Transition Metal Carbides (MXenes): A Combined Experimental/Theoretical ^{13}C Solid State NMR Approach

Florian Brette, Dani Kourati, Michael Paris, Lola Louprias, Stéphane Célérier, Thierry Cabioc'H, Michael Deschamps, Florent Boucher, Vincent Mauchamp

► To cite this version:

Florian Brette, Dani Kourati, Michael Paris, Lola Louprias, Stéphane Célérier, et al.. Assessing the Surface Chemistry of 2D Transition Metal Carbides (MXenes): A Combined Experimental/Theoretical ^{13}C Solid State NMR Approach. *Journal of the American Chemical Society*, 2023, 145 (7), pp.4003-4014. 10.1021/jacs.2c11290 . hal-04012767

HAL Id: hal-04012767

<https://hal.science/hal-04012767>

Submitted on 3 Mar 2023

HAL is a multi-disciplinary open access archive for the deposit and dissemination of scientific research documents, whether they are published or not. The documents may come from teaching and research institutions in France or abroad, or from public or private research centers.

L'archive ouverte pluridisciplinaire **HAL**, est destinée au dépôt et à la diffusion de documents scientifiques de niveau recherche, publiés ou non, émanant des établissements d'enseignement et de recherche français ou étrangers, des laboratoires publics ou privés.

Assessing the surface chemistry of 2D transition metal carbides (MXenes): a combined experimental/theoretical ^{13}C solid state NMR approach

Florian Brette,^{1,2} Dani Kourati,³ Michael Paris,² Lola Louprias,⁴ Stéphane Célrier,⁴ Thierry Cabioch,¹ Michael Deschamps,³ Florent Boucher,^{2*} Vincent Mauchamp^{1*}

¹ UNIVERSITE DE POITIERS, ISAE-ENSMA, CNRS, PPRIME, 86073 POITIERS, FRANCE

² NANTES UNIVERSITE, CNRS, INSTITUT DES MATERIAUX DE NANTES JEAN ROUXEL, IMN, F-44000 NANTES, FRANCE

³ CNRS, CEMHTI UPR3079, UNIVERSITE D'ORLEANS, 45071 ORLEANS, FRANCE

⁴ INSTITUT DE CHIMIE DES MILIEUX ET MATERIAUX DE POITIERS (IC2MP), UNIVERSITE DE POITIERS, CNRS, F-86073 POITIERS, FRANCE

ABSTRACT: The surface functionalization of 2D transition metal carbides or nitrides, so-called MXenes, is one of the fundamental levers allowing to deeply modify their physicochemical properties. Beyond new approaches to control this pivotal parameter, the ability to unambiguously assess their surface chemistry is thus key to expand the application fields of this large class of 2D materials. Using a combination of experiments and state of the art density functional theory (DFT) calculations, we show that the NMR signal of the carbon - the element common to all MXenes carbides and corresponding MAX phase precursors - is extremely sensitive to the MXenes functionalization although carbon atoms are not directly bonded to the surface groups. The simulations include the orbital part to the NMR shielding and the contribution from the Knight Shift which is crucial to achieve good correlation with the experimental data, as demonstrated on a set of reference MXene precursors. Starting with the $\text{Ti}_3\text{C}_2\text{T}_x$ MXene benchmark system, we confirm the high sensitivity of the ^{13}C NMR shift to the exfoliation process. Developing a theoretical protocol to straightforwardly simulate different surface chemistries, we show that the ^{13}C NMR shift variations can be quantitatively related to different surface compositions and number of surface chemistry variants induced by the different etching agents. In addition, we propose that the etching agent not only affect the nature of the surface groups but also their spatial distribution. The direct correlation between surface chemistry and ^{13}C NMR shift is further confirmed on the V_2CT_x , Mo_2CT_x and Nb_2CT_x MXenes.

▪ INTRODUCTION

Since the discovery of graphene,¹ 2D materials have become a major interest in materials science, physics and chemistry because of their unique properties and countless potential applications. Among the large variety of 2D systems discovered since then, bidimensional transition metal carbides or nitrides – so-called MXenes where M denotes a transition metal and X is either C or N^{2,3} – occupy a very particular place for different reasons. First, MXenes exhibit metallic electrical conductivity which is quite unusual in the 2D world where one essentially finds semi-metals, semi-conductors or insulators. In addition, MXenes being obtained from the chemical exfoliation of the A-element (essentially from groups 13 and 14 of the periodic table) from the MAX phases,⁴ a family of more than 150 nanolaminated ternary carbides/nitrides or corresponding solid solutions,⁵ their chemistry is potentially extremely large (see fig. 1 for MAX phases structure). The M or X elements can thus be modified by changing the MAX phase precursor with major consequences in terms of properties like, *e.g.* the possibility to turn their metallic electrical behavior into semiconductor-like.⁶ Since the synthesis in 2011 of Ti_3C_2 ,⁷ the first and most

studied MXene to date,⁸ more than 40 different MXene compositions have been reported. In addition, depending on the MAX phase, the elementary thickness of the MXene layers can be changed from three to nine (M, X) atomic planes, making these materials a unique platform for the study of the structure/chemistry/properties correlation in 2D. Finally, depending on the etching process used to convert the MAX phase bulk material into 2D flakes, MXenes can demonstrate a pronounced hydrophilic character which enables their easy processing and make them behaving as 2D conductive clays.⁹ Because of this unique combination of properties, MXenes have been reported to exhibit outstanding characteristics for a very large range of applications covering energy storage,¹⁰ electromagnetic interference shielding,¹¹ sensing,¹² transparent conducting electrodes¹³ or membranes¹⁴ among many others.

Beyond the (M, X) composition and layer thickness, MXene properties are also largely influenced by their surface chemistry inherited from the exfoliation process. MXene chemical formula are then given by $\text{M}_{n+1}\text{X}_n\text{T}_x$, where the n index (varying from 1 to 4 – see figure 1) determines the layer thickness, and with the T surface functionalization

groups being usually a mix of O, OH, F and/or Cl in the most common cases. These T-groups play a vital role in many respects: they govern the interactions between MXene layers in multilayer stacks,¹⁵ they are expected to play a major role in the interaction between the MXene sheets and different environments such as gases^{16,17} or other functional molecules/materials, which is key for the design of advanced composites.^{18,19} Being directly bonded to the outer M elements, the *d*-electrons of which have a major contribution at the Fermi level, the T-groups have been consequently identified as key elements for deeply modifying the electronic structure and related properties of MXene layers with the possibility, for instance, to induce superconductivity or control their magnetic state.²⁰⁻²² Given the huge possibilities offered by this lever in expanding the properties and application field of MXenes, lots of efforts have been devoted to the modification of MXenes surface chemistry, with the ultimate goal of controlling it. This can be done by playing with the exfoliation process which has a strong impact on the ratio between the different T-groups for a given MAX precursor, and can even promote single termination types.^{21,23,24} It can also be achieved through post-treatments like, *e.g.* thermal annealing or reaction in various atmospheres.^{25,26} In order to take full advantage of the possibilities offered by the surface chemistry of MXenes,²⁷ other complementary alternatives must be developed.

As a direct consequence, the quantitative characterization of MXenes surface chemistry appears as a major, and still very challenging, issue. It has been tackled using different techniques like X-ray photoelectron spectroscopy (XPS),^{24,25,28} transmission electron microscopy and associated spectroscopies,²⁹⁻³² neutron scattering,³³ or Raman spectroscopy^{34,35} among others. Generally speaking, the quantification of surface groups obtained for *a priori* similar MXenes can differ quite substantially depending on the used approach. There are many possible reasons for that, including differences in the etching/drying protocols or MAX phase precursors resulting in different surface chemistries, different probed volumes (*e.g.*, quite large surfaces corresponding to the topmost atomic layers in XPS, nanometer scale areas in TEM), or difficulties in the interpretation of the collected data due to the presence of impurities or intercalated species between the layers. In this context, nuclear magnetic resonance (NMR) spectroscopy appears as a very powerful technique allowing to characterize complex, potentially disordered, materials at the molecular level over different time scales and with elemental selectivity. It proved to provide detailed structural information with extreme sensitivity to different kinds of structural defects for all types of materials including 2D ones,³⁶⁻³⁸ and has thus also been used on MXenes.³⁹⁻⁴³ Like for many other materials, the interpretation of NMR spectra on MXenes often relies on the comparison with reference spectra to identify the contribution from impurities or interpret the observed NMR shifts. In this respect, and because of their very good electrical conductivity, the mechanisms involved in NMR shielding are rather complex, mixing orbital screening and Knight shifts in non-determinable proportions from the experimental point of view. NMR simulations based on density functional theory (DFT) calculations allow the computation of NMR shielding,^{44,45} with nowadays the inclusion of Knight shifts,⁴⁶⁻⁴⁸ an essential contribution for MXenes which has

never been considered so far to the best of our knowledge. It is thus the purpose of the present study to show how the analysis of NMR shifts in MXenes can be achieved with these simulations, paving the way towards a more systematic use of NMR in the MXene community.

The NMR studies published to date on MXenes focused on different kinds of nuclei including those related to the surface groups (¹H, ¹⁹F), the transition metal when possible (*e.g.*, ⁹³Nb for Nb-based systems) and the carbon atoms.^{39-43,49,50} In addition, some studies also focused on the NMR signature of intercalated species (*e.g.*, ⁷Li, ²³Na, ²⁹Si) in order to investigate intercalation mechanisms in MXene stacks.^{51,52} Focusing only on the spectra of the elements from the MXene structure, *i.e.* the M, X or T elements, the ¹³C has been shown to be sensitive to the MAX to MXene transformation,^{39,40,42} and to the exfoliation process.^{40,41} As we will show, it carries a lot of information on the MXene surface chemistry provided that an unambiguous analysis can be performed. In addition, the ¹³C NMR spectra are generally simpler to interpret than those of the T-groups, the other elements common to most MXenes, which generally exhibit multiple contributions ascribed to side products of the exfoliation process or intercalated species.^{40,42,43} The present study thus focuses on the quantitative analysis of the ¹³C NMR signature as a general probe of the MXene surface chemistry with high sensitivity. By comparing state of the art DFT simulations including the Knight shift contribution for the calculation of the NMR shielding, with experiments on different MAX phases (as a first group of reference materials) and then MXenes, we show that the ¹³C NMR shifts are directly related to the nature of surface groups in MXenes. In addition, because of its high sensitivity and its ability to probe large volumes as compared to other techniques like, *e.g.* XPS or TEM, a large-scale analysis of the sample can be obtained and different composition variants can be identified and quantified. Finally, we show that the ¹³C NMR shielding mechanisms are very different from one MXene to another, as well as for the corresponding MAX phases, so that DFT simulations like those provided in the present study offer major contributions to the NMR spectra analysis in this large class of 2D materials.

■ METHODS SECTION

MAX phases and MXene synthesis are described in supporting information, part S1.

DFT simulations: structural models. All MAX phases were described in the P6₃/mmc space group considering unit cell parameters fixed to their experimental values and relaxed atomic positions. MXenes were described as single layers considering around 18 Å vacuum between the layers. For all the investigated MXenes, atomic positions were relaxed keeping the in-plane unit cell parameters fixed to their experimental values (the *c* parameter value was imposed to get the previously mentioned 18 Å vacuum between the layers), as described later in the text. The structures of model systems with a single type of surface termination, corresponding to a M_{n+1}X_nT₂ chemical formula, were described in the P6₃/mmc space group too. When considering more complicated surface chemistries, *i.e.* mixed surface groups, the unit cell symmetry had to be reduced.

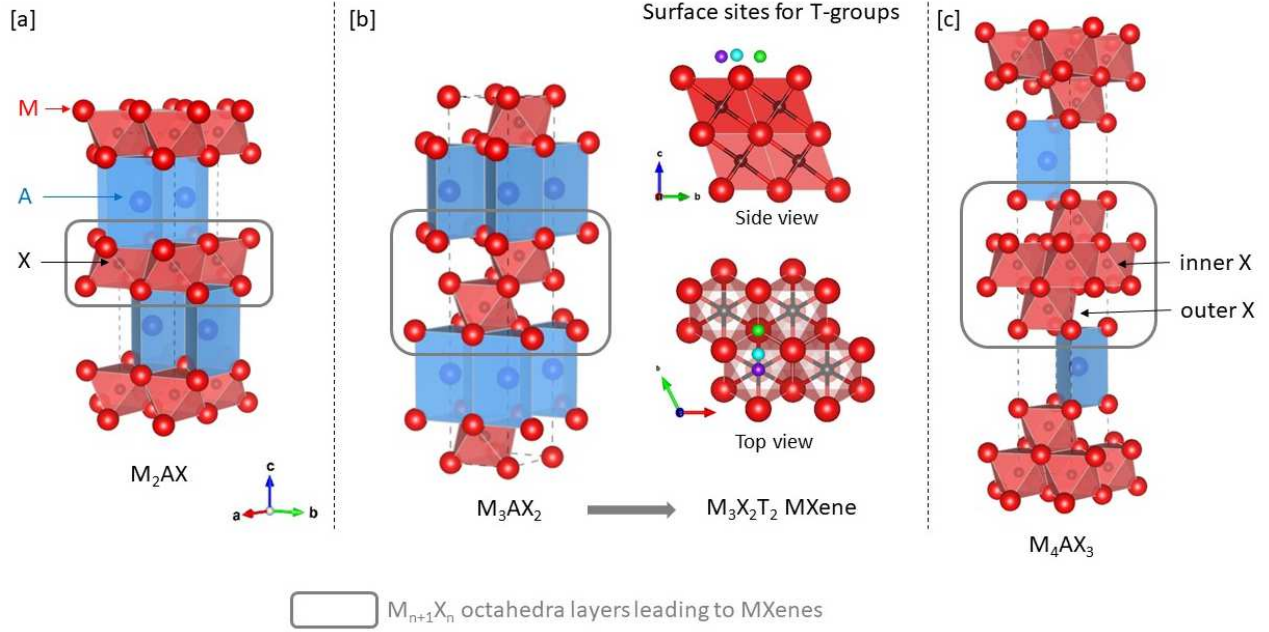


Figure 1. Crystallographic structures of MAX phases with $n = 1$ [a], 2 [b], 3 [c] octahedra layers (highlighted in grey) between the A elements layers (in blue). The octahedra layers forming the skeleton of the corresponding MXene are circled in grey. The M element is represented as red spheres and the X element as black ones. In [b] the three different sites considered for the T groups on MXenes' surface are given: FCC (green), HCP (purple) and Bridge (cyan). In order to ease their identification, only one surface group is sketched in these structural models but all calculations were performed on fully functionalized surfaces, *i.e.* corresponding to $M_{n+1}X_nT_2$ compositions (with T = -O, -OH, -F or -Cl) – see SI, part S2. One should notice that the Mo_2Ga_2C structure is different from those of the MAX phases with a double A element layer between the octahedral layers. Structural models were drawn with VESTA software.⁵⁴

Depending on the nature of M, the most stable site on the MXenes surface for the T groups may change. There are two typical configurations corresponding to an FCC and an HCP site, as well as an experimentally reported Bridge position,^{25,53} as depicted in figure 1-b for $Ti_3C_2T_2$. The most stable site, according to our DFT simulations, was considered for each MXene with FCC positions for $Ti_3C_2T_2$, V_2CT_2 and Nb_2CT_2 and an HCP position for Mo_2CT_2 . In all cases, excepted for the pristine systems corresponding to $M_{n+1}X_n$ compositions, the MXene layers were described considering fully functionalized surfaces as usually done in simulations^{55,56} and in agreement with many XPS quantifications²³. The structural models corresponding to the $Ti_3C_2O_2$ system with different surface groups positions (FCC, HCP or bridge), as well as those corresponding to the other $M_{n+1}X_nO_2$ ideal systems are represented in SI part S2. Some of the models corresponding to mixed surface terminations in the $Ti_3C_2(O_xF_y)_2$ systems are represented in SI, part S9. The unit cell parameters used for the calculations are given in table S3-a for MAX phases and MXenes.

The structural relaxations of the MAX phases and most MXenes were performed with the WIEN2k code.^{57,58} We used 2000 k-points in the first Brillouin zone (BZ) for all systems and a RK_{max} value of 7.5. The free parameters of the atoms were relaxed with a convergence criterion of 1.0 mRy/a.u. The -(OH) terminated MXenes structural relaxations were done with the VASP code, using the projector augmented wave method (PAW).^{59,60} Standard GGA PAW potentials, taken from the VASP database, were used for the

calculations. They are given in SI, part S4. We used a plane-wave cutoff energy of 500 eV. The free internal coordinates of the atoms were optimized in order to reduce the magnitude of the force acting on each atom to less than 0.01 eV/Å. The Brillouin zone was sampled using a set of 10x10x2 Monkhorst-Pack k-points grid.

DFT simulations: NMR simulations with WIEN2k. We will start with a short description of the calculated quantities, more details can be found in the papers of Laskowski *et al.*^{46–48} who implemented the approach used here. The key quantity in the simulations is the NMR shielding tensor $\vec{\sigma}$ connecting the induced magnetic field \mathbf{B}_{ind} at the nucleus at site \mathbf{R} to the external uniform magnetic field \mathbf{B}_0 . It is defined as follows:

$$\mathbf{B}_{ind}(\mathbf{R}) = -\vec{\sigma}(\mathbf{R})\mathbf{B}_0 \quad (\text{eq. 1})$$

In metals, the induced field has two distinct contributions: the orbital part - \mathbf{B}_{orb} - leading to the orbital contribution of the shielding, σ_{orb} , which is related to the NMR chemical shift, and the spin part leading to the spin contribution to the shielding, σ_{spin} , which is related to the Knight Shift. \mathbf{B}_{orb} is obtained from the Biot-Savart's law (in atomic units):

$$\mathbf{B}_{orb} = \frac{1}{c} \int d^3\mathbf{r} \mathbf{j}_{ind}^{orb}(\mathbf{r}) \times \frac{\mathbf{R}-\mathbf{r}}{|\mathbf{R}-\mathbf{r}|^3} \quad (\text{eq. 2})$$

Table 1. Calculated orbital σ_{orb} , spin σ_{spin} , and isotropic σ_{iso} , shieldings compared to the measured NMR shifts δ_{exp} for the set of eleven ^{13}C data obtained on our data set. The error on our experimental data, *i.e.* the spectra recorded on Ti_2AlC , Ti_3AlC_2 , $\text{Mo}_2\text{TiAlC}_3$, $\text{Mo}_2\text{Ti}_2\text{AlC}_3$ and $\text{Mo}_2\text{Ga}_2\text{C}$, is estimated to be ± 10 ppm. This value is mainly due to the dispersion of the data recorded on different batches of the same material. The spin contribution includes both the contact, σ_c , and dipolar, σ_{dip} , terms. The deduced isotropic NMR shifts - δ_{iso} - obtained from equation 5 are given in the sixth column. In this last column, the absolute value of the relative error with respect to the experimental data ($|\text{err}| = |\delta_{\text{iso}} - \delta_{\text{exp}}| / \delta_{\text{exp}} * 100$) is also given in brackets for each compound. The average value calculated from these data gives a 15% relative error, which will be considered as the uncertainty of our simulations (the average absolute error on this data set is 42 ppm). For the spin and orbital components, the dependence of the shielding on the “smearing” in ppm/mRy, and computed as $[\sigma(\text{T}_1) - \sigma(\text{T}_2)] / (\text{T}_1 - \text{T}_2)$ with $\text{T}_1 = 8$ mRy and $\text{T}_2 = 4$ mRy, is given in square brackets. The small values obtained show the good convergence of the calculations with respect to the smearing parameter.

Material	σ_{orb}	σ_{spin}	σ_{iso}	δ_{exp} (ppm)	δ_{iso} (ppm)
TiC	-371 [10]	-5 [1]	-376	527 ⁴⁰	523 (0.8 %)
Ti_2AlC	-428 [0]	116 [4]	-312	521	465 (10.7 %)
Ti_3AlC_2	-464 [0]	106 [1]	-358	552	506 (8.3 %)
$\text{Mo}_2\text{TiAlC}_2$	-208 [-1]	57 [-11]	-151	270	319 (18.2 %)
$\text{Mo}_2\text{Ti}_2\text{AlC}_3$ (inner)	-234 [0]	-22 [-3]	-256	353	414 (17.3 %)
$\text{Mo}_2\text{Ti}_2\text{AlC}_3$ (outer)	-237 [0]	26 [2]	-211	315	373 (18.5 %)
$\text{Mo}_2\text{Ga}_2\text{C}$	-202 [0]	142 [2]	-61	176	238 (35.2 %)
V_2AlC	-310 [0]	342 [-5]	32	208 ³⁹	154 (26 %)
Nb_2AlC	-223 [0]	99 [-4]	-124	293 ⁴²	295 (0.6 %)
Nb_4AlC_3 (inner)	18 [-1]	-45 [0]	-26	238 ⁴²	207 (13 %)
Nb_4AlC_3 (outer)	-190 [0]	79 [2]	-111	324 ⁴²	283 (12.6 %)

where the induced orbital current $\mathbf{j}_{\text{ind}}^{\text{orb}}(\mathbf{r})$ is obtained in a linear response approach.^{44,45,61} The spin contribution is computed using the magnetic hyperfine field⁶² which has two contributions, the Fermi contact term - \mathbf{B}_c - and the spin-dipolar contribution - \mathbf{B}_{dip} -. These two quantities are given as follows:

$$\mathbf{B}_c = \frac{8\pi}{3} \mathbf{m}_{\text{av}} \quad (\text{eq. 3})$$

$$\mathbf{B}_{\text{dip}} = \int \frac{S(r)}{r^3} [3(\mathbf{m}(r)\hat{\mathbf{r}})\hat{\mathbf{r}} - \mathbf{m}(r)] d^3r \quad (\text{eq. 4})$$

with \mathbf{m}_{av} the average spin density over a region near the nucleus (within the Thomson radius from the nucleus), and $S(r)$ the reciprocal of the relativistic mass enhancement. The spin contribution to the shielding is then: $\sigma_s = -\mathbf{B}_c/B_0 - \mathbf{B}_{\text{dip}}/B_0$.

These quantities were calculated using the all-electron, full potential augmented-plane-wave (APW) method as implemented in the WIEN2k code.^{57,58} In most calculations, exchange and correlation effects were treated in the

generalized gradient approximation (GGA) using the Perdew Burk Ernzerhof functional.⁶³ Calculations presented in the paper were performed in a scalar relativistic framework. Calculations in a fully relativistic framework, as well as considering an onsite exact exchange approximation, were also performed on $\text{Mo}_2\text{Ga}_2\text{C}$, $\text{Mo}_2\text{TiAlC}_2$, V_2AlC and $\text{Ti}_3\text{C}_2\text{O}_2$, without significant changes in terms of electronic structure (see SI - parts S5 and S6). For all calculations the plane wave basis set was defined using a RK_{max} value of 7.5, except for -(OH) terminated MXenes where it was reduced to 3.5 due to shortest O-H bonds. The muffin-tin radii associated with the different elements of the materials under consideration were obtained from the automated routine provided with WIEN2k.

The orbital and spin components of the induced magnetic field are very sensitive to the details of the Fermi surface, and so require a very dense sampling of the Brillouin zone (BZ). In MAX phases we used a Monkhorst-Pack⁶⁴ k-point grid of around $60 \times 60 \times z$, with $6 < z < 12$ depending on the c lattice parameter, in the first BZ for all systems. In MXenes, considering their intrinsic 2D nature, we used a k-point grid of around $60 \times 60 \times 1$. A ‘smearing parameter’ of 8 mRy was used to ensure consistency and converged calculations. The convergence of the NMR shielding as a function the number

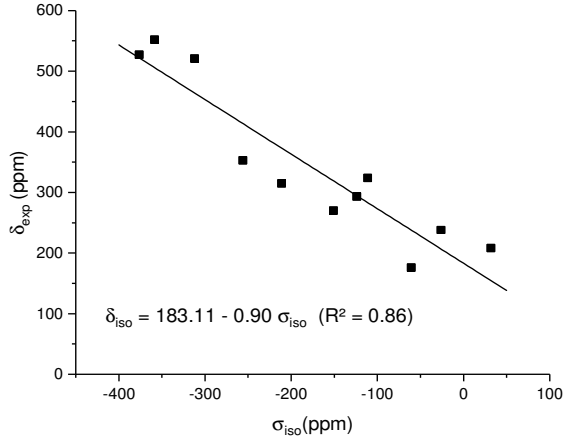


Figure 2. Correlation between the calculated shielding σ_{iso} in the reference materials (Ti_2AlC , Ti_3AlC_2 , $\text{Mo}_2\text{TiAlC}_2$, $\text{Mo}_2\text{Ti}_2\text{AlC}_3$, $\text{Mo}_2\text{Ga}_2\text{C}$, V_2AlC , Nb_2AlC , Nb_4AlC_3 and TiC) and the experimental NMR shift δ_{exp} . The linear regression for this set of data is also given together with the R^2 value. It allows to determine the calculated NMR shifts δ_{iso} .

of k-points in the first Brillouin zone is illustrated in SI, part S4, for representative examples: Ti_3AlC_2 and $\text{Ti}_3\text{C}_2\text{O}_2$. The dependence of the calculation to the smearing parameter is given in square brackets in the second and third columns of table 1. It is shown to be weak, below 11 ppm, for all materials showing well converged calculations. As expected, the smearing parameter mainly affects the spin contribution.⁴⁶⁻⁴⁸ With such parameters the two components of the NMR shielding are converged within ± 5 ppm. Due to the experimental conditions used to acquire the ^{13}C NMR signal (see below), only the isotropic part of the chemical shift was obtained, so that only the isotropic part of the shielding (σ_{iso}) was simulated.

NMR measurements. As the samples are conductive, magic angle spinning (MAS) is difficult. To limit conductivity issues, our samples were diluted in boron nitride in order to decrease the samples overall conductivity. Boron nitride (chempur 98.5+%) was dried in an oven at 200°C for two days to remove water molecules. Boron nitride was chosen as it mixes well with our samples and did not yield spurious signals in our spectra as observed in the ^{13}C spectrum of MXenes mixed with potassium bromide. After several tests, a 50/50 ratio by mass is optimal for our systems. The mixture was then ground in a mortar until it appeared homogeneous and used to fill a Bruker 4 mm ZrO_2 rotor.

MAS-NMR ^{13}C spectra were acquired using a Bruker Avance III spectrometer operating at a magnetic field of 7.02 T (corresponding to a Larmor ^1H frequency of 300 MHz), equipped with a Bruker DVT 4 mm magic angle spinning probe. The ^{13}C experiments were performed at 9 kHz MAS with a Carr-Purcell-Meiboom-Gill (CPMG) echo train pulse sequence,⁶⁵ which allowed us to obtain a better signal-to-noise despite the long relaxation time T_1 and the low natural abundance of ^{13}C . The ^{13}C spectra were acquired with a radio-frequency field strength of 70 kHz ($t_{90} = 3.57 \mu\text{s}$ for the $\pi/2$ pulse). We chose a recycling delay of 10 s as done by Hope *et al.*⁴⁰ For each transient, 128 echoes are recorded

with 18 rotor periods per echo, and 16k transients were recorded in total. Each echo signal was stored in a separate FID in a 2D experiment, and Fourier transform of the full echoes were performed in the direct dimension, using a 1000 Hz Gaussian line broadening function. All the full echo spectra were then summed together to obtain the ^{13}C spectrum. A tetramethylsilane (TMS) solution was used as a reference for the ^{13}C chemical shift. The data was analyzed using the TopSpin software (TopSpin 4.1.4). Finally, the DMfit program was used for peak fitting.⁶⁶

RESULTS AND DISCUSSION

MAX phases: from the theoretical shielding σ_{iso} to the experimental NMR shift δ_{exp} . Experimentally, the NMR shift is determined with respect to a reference. In order to compare simulations with experiments in the case of MXenes, one has thus to obtain the correlation law between the calculated isotropic shielding σ_{iso} and the experimental isotropic NMR shifts δ_{exp} . To do so the linear relationship converting the calculated shielding σ_{iso} to a calculated NMR shifts δ_{iso} , directly comparable to the experimental NMR shifts δ_{exp} , should be determined.⁴⁶⁻⁴⁸ Such a linear relationship can be obtained considering a set of reference materials. In our case, we have naturally chosen Al-based MAX phases and $\text{Mo}_2\text{Ga}_2\text{C}$ as reference materials, together with TiC , in order to next discuss and analyze the ^{13}C in MXenes. In addition to being the precursors for MXenes, MAX phases and $\text{Mo}_2\text{Ga}_2\text{C}$ are expected to have well-defined crystallographic structures and chemistries as compared to MXenes, where the surface chemistry and side-products inherited from the exfoliation process complexify the structure in a given multilayer stack. A dataset of ^{13}C NMR experimental shifts was thus built combining data from the literature obtained on V_2AlC , Nb_2AlC , Nb_4AlC_3 , Ti_3AlC_2 and TiC with our measurements performed on Ti_2AlC and Mo-based MAX phases - namely $\text{Mo}_2\text{TiAlC}_2$, $\text{Mo}_2\text{Ti}_2\text{AlC}_3$ - and $\text{Mo}_2\text{Ga}_2\text{C}$ (the corresponding spectra are given in SI - part S7). This set of data allows considering MAX phases with different transition metals and n indexes (see figure 1). In addition, one can distinguish between two carbon crystallographic sites, so-called inner and outer in figure 1-c, in a given structure for the $\text{Mo}_2\text{Ti}_2\text{AlC}_3$ and Nb_4AlC_3 413 MAX phases. Overall, this gives eleven experimental points to be compared with the corresponding simulations.

The comparison between the calculated isotropic shielding σ_{iso} and the experimental isotropic NMR shifts δ_{exp} are given in the fourth and fifth columns of table 1 and plotted in figure 2, evidencing the expected linear correlation between these two quantities. The linear least square fit obtained from this data set gives the following relation:

$$\delta_{\text{iso}} = 183.11 - 0.90 \sigma_{\text{iso}} \quad (\text{eq. 5})$$

with an R^2 of 0.86 showing a rather good correlation. The value of the slope in this relation, *i.e.* -0.90, is close to the ideal value of -1 and is satisfactory for GGA-PBE calculations. Using equation 5, it is now possible to obtain the theoretical δ_{iso} for each material and compare it to the δ_{exp} as done in the sixth column of table 1. In this column are also

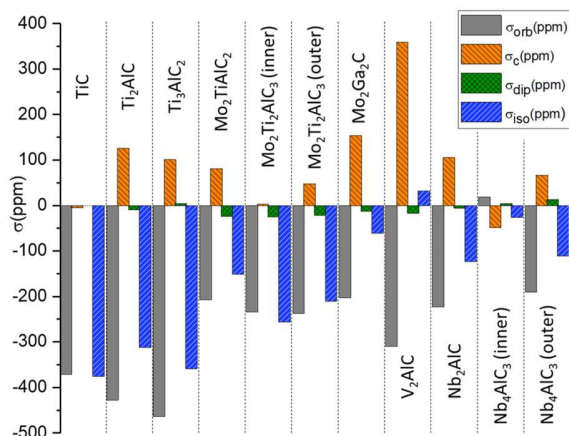


Figure 3. Calculated orbital σ_{orb} (grey) and spin components to the shielding, the latter being the sum of the contact term σ_c (orange with black stripes) and the spin-dipolar contribution σ_{dip} (green with black stripes). The resulting total contribution calculated for the ^{13}C isotropic shielding σ_{iso} in Ti_2AlC , Ti_3AlC_2 , $\text{Mo}_2\text{TiAlC}_2$, $\text{Mo}_2\text{Ti}_2\text{AlC}_3$, $\text{Mo}_2\text{Ga}_2\text{C}$, V_2AlC , Nb_2AlC , Nb_4AlC_3 and TiC is given in blue with white stripes. The corresponding numerical data for σ_{orb} and σ_{iso} can be found in table 1. The numerical values for the contact term, σ_c , and the dipole contribution, σ_{dip} , can be found in table S8.

given in brackets the absolute values of the relative errors between the δ_{exp} and δ_{iso} for each compound. The mean value calculated from this set of relative errors is 15%, which will be taken as an estimate of the uncertainty of our simulations. This value, although a little higher, is similar to that reported by Khoo *et al.*⁴⁸ for the Al and Sc NMR shielding in Heusler phases using the same approach.

Before analyzing the ^{13}C NMR shielding in MXenes, we propose a short discussion on the shielding mechanism in our reference materials. As expected from their intrinsic metallic character, the NMR shielding is a combination of both the orbital and spin components. These two contributions are of opposite sign for almost all compounds, but TiC and the inner carbon crystallographic site in $\text{Mo}_2\text{Ti}_2\text{AlC}_3$, as can be seen in the two first columns of table 1 and summarized in figure 3. The relative contribution of these two components to the isotropic shielding σ_{iso} changes significantly from one phase to another but some general trends can be observed. σ_{orb} is generally larger than σ_{spin} although the spin part has a very significant contribution for almost all MAX phases studied here, pointing out the absolute necessity to take this latter contribution into account to reproduce experimental data. For V_2AlC , it is even greater than the orbital part. In addition, as detailed in SI (table S8), the spin contribution is usually dominated by the contact term, the dipolar term being generally smaller. Moreover, one can observe that the spin contribution generally has a diamagnetic behavior (positive value) whereas the orbital part has a paramagnetic contribution (negative value). Finally, it is to be noted that the orbital part of the shielding is rather different from one phase to another evidencing the complexity of these materials and the role played by the chemical

Table 2. Calculated ^{13}C NMR shielding for the three surface group sites, FCC, HCP and Bridge on $\text{Ti}_3\text{C}_2\text{O}_2$

	σ_{orb}	σ_{spin}	σ_{iso}	δ_{iso} (ppm)
$\text{Ti}_3\text{C}_2\text{O}_2$ (FCC)	-376	-46	-422	564
$\text{Ti}_3\text{C}_2\text{O}_2$ (HCP)	-335	-45	-381	526
$\text{Ti}_3\text{C}_2\text{O}_2$ (Bridge)	-387	-1	-388	533

composition and the structure (*i.e.* the value of n) on the carbon electronic structure in MAX phases.

Having a closer look at the data in table 1, one can notice that for two particular compounds, *i.e.* $\text{Mo}_2\text{Ga}_2\text{C}$ and V_2AlC , the calculated NMR shifts are far from the measured values with relative errors of 35.2% and 26%, respectively. For both cases, fully relativistic and onsite exact exchange calculations were conducted in order to test possible improvements of the simulations. No significant changes in terms of electronic structure were obtained (see SI - parts S5 and S6). Looking for another possible explanation, one can notice that in these systems σ_{spin} has a very high contribution to the NMR shift. Given that this contribution comes from conduction electrons, one can reasonably assume that any deviation from the ideal stoichiometry we have considered will modify the valence filling and thus the density of states at the Fermi level leading to a significant change in δ_{exp} . The chemical composition of the $\text{Mo}_2\text{Ga}_2\text{C}$ powders was thus investigated using Inductively Coupled Plasma Optical Emission Spectroscopy. The obtained chemical composition, normalized to two Mo, is $\text{Mo}_2\text{Ga}_{1.90}\text{C}_{0.75}$ evidencing important sub-stoichiometries on both the Ga and C sites (the quantification of the carbon content should be considered with care). This could be an explanation for the large difference between experiments and calculations. Concerning the V_2AlC data which were taken from the literature³⁹, we could not find any chemical composition in the paper. However sub-stoichiometries on the Al or C sites could also be envisaged as an explanation for the strong deviation between the experimental and theoretical values. The effect would be particularly important for V_2AlC since the DOS has a peak at the Fermi level, as shown in SI - part S5, which make the corresponding calculation very sensitive to chemical composition changes.⁴⁷ Finally, one can observe that the shift differences calculated between the two inequivalent carbon atoms in the 413 structures (so-called inner and outer in figure 1-c) are in very good agreement with those obtained experimentally.

Given the good agreement obtained between the calculated NMR shifts δ_{iso} and the measured experimental NMR shifts δ_{exp} in MAX phases, the established linear relation will now be used to determine δ_{iso} from the σ_{iso} in MXenes in order to analyze the role of the functionalization on the ^{13}C NMR spectra.

MXenes surface chemistry from ^{13}C solid state NMR. Using the methodology developed above in structurally

Table 3. ^{13}C δ_{iso} values obtained for different surface functionalizations in the $\text{Ti}_3\text{C}_2\text{T}_x$ system (last column). The decomposition into the orbital and spin contributions is given together with the corresponding σ_{iso} .

	σ_{orb}	σ_{spin}	σ_{iso}	δ_{iso} (ppm)
$\text{Ti}_3\text{C}_2\text{O}_2$ (FCC)	-376	-46	-422	564
$\text{Ti}_3\text{C}_2\text{F}_2$ (FCC)	-289	142	-147	315
$\text{Ti}_3\text{C}_2(\text{OH})_2$ (FCC)	-288	115	-173	339
$\text{Ti}_3\text{C}_2\text{Cl}_2$ (FCC)	-288	121	-167	334
Ti_3C_2	-410	-253	-663	781

well-defined materials and the corresponding determined linear relationship, we proceed with the comparative study of NMR experimental spectra and calculated shielding in MXenes. We compare experimental and calculated NMR shieldings in $\text{Ti}_3\text{C}_2\text{T}_x$, Nb_2CT_x , V_2CT_x , Mo_2CT_x MXenes, to give a quite general picture for the MXene family.

$\text{Ti}_3\text{C}_2\text{T}_x$: the benchmark MXene. We first focus on the $\text{Ti}_3\text{C}_2\text{T}_x$ benchmark material to determine the main structural parameters affecting the simulation of the ^{13}C NMR shifts and find relevant approaches for their description. We will mainly focus on two important aspects: 1) the importance of the surface site for a given termination T, and 2) the influence of a mixture of different surface terminations T and T'. Considering the first point, and as mentioned before, there are typically three different sites to be considered for the surface terminations on $\text{Ti}_3\text{C}_2\text{T}_x$ (see figure 1-b and SI – part S2), *i.e.* directly on top of the transition metal atoms in the center of the sheet (FCC), on top of the sub-layer X element (HCP) and finally the Bridge site. We therefore analyzed the influence of the surface group positions on the calculated ^{13}C NMR shielding to determine the effects of the different surface group sites on peak displacements.

Table 2 reports the calculated isotropic value of NMR shielding for three different types of -O termination positions of in the $\text{Ti}_3\text{C}_2\text{O}_2$ MXene. The orbital and spin contributions are also given, as well as the corresponding NMR shifts δ_{iso} deduced from equation 5. Only small differences are observed between these three positions, with at most 52 ppm on the orbital component and 45 ppm on the spin component, which results in a 38 ppm maximum difference on the calculated NMR shift δ_{iso} . This difference represents a relative error of around 7% with respect to the calculated δ_{iso} values, which is lower than the 15% estimated uncertainty determined on our correlation curve from MAX phases and discussed in table 1. In addition, the 38 ppm difference is very similar to the intrinsic width of the ^{13}C NMR peaks recorded on $\text{Ti}_3\text{C}_2\text{T}_x$ (see figure 5 discussed later and SI – part S10). We will therefore consider, as a first approximation,

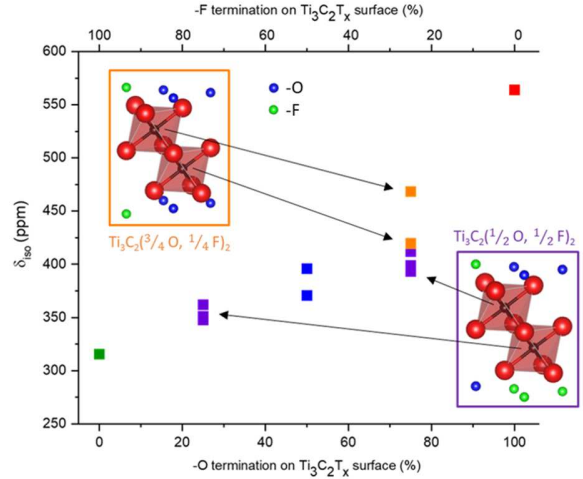


Figure 4. Calculated ^{13}C NMR shifts δ_{iso} in different $\text{Ti}_3\text{C}_2\text{O}_{2-x}\text{F}_x$ ($0 < x < 2$) for the carbon atoms in different structures and represented as a function of the composition of the nearest surface from the investigated carbon atom. In the structural models, the F (O) atoms are displayed as green (blue) spheres. For more detailed visualization of the structures corresponding to the $\text{Ti}_3\text{C}_2(\text{O}_{3/4}\text{F}_{1/4})_2$ and $\text{Ti}_3\text{C}_2(\text{O}_{1/2}\text{F}_{1/2})_2$ see SI – part S9.

that the positions of the surface groups on the MXenes sheet do not greatly affect the calculated NMR shifts. Experimentally, and considering the intrinsic width of the NMR peaks as discussed later, the different termination sites should therefore not generate new peaks in the NMR spectra, but may instead lead to a slight broadening of the spectral signatures. The NMR shifts will then be calculated considering only the most stable position for $\text{Ti}_3\text{C}_2\text{T}_x$, the FCC one in the present case.

A second important point when describing MXene surfaces is to evaluate the influence of a mixture of terminations. Considering that in model $\text{Ti}_3\text{C}_2\text{T}_2$ compounds with T = -O, -F, -(OH) or -Cl terminations, the theoretical NMR shifts δ_{iso} are 564, 315, 339 and 334 ppm, respectively (see table 3), the effect of a mixed arrangement on the surface was investigated considering a mixture of -O and -F terminations as their calculated NMR shifts are the further apart (in addition, NMR shifts corresponding to -F, -(OH) or -Cl groups are very close). ^{13}C NMR shifts δ_{iso} were thus calculated in solid solutions, changing the -O to -F ratio onto the surfaces with the following target compositions: $\text{Ti}_3\text{C}_2\text{F}_{1.5}\text{O}_{0.5}$, $\text{Ti}_3\text{C}_2\text{F}_1\text{O}_1$, $\text{Ti}_3\text{C}_2\text{F}_{0.5}\text{O}_{1.5}$. Since NMR is a probe of the local order at a very short range, the NMR shifts are discussed according to the composition of the nearest surface from the investigated carbon atom (see the structural models given in fig. 4 and SI part S9). As an example, the purple rectangle in fig. 4 shows a model compound having an average $\text{Ti}_3\text{C}_2\text{F}_1\text{O}_1$ composition, with two distinct signals for the two C atoms depending of their proximity to either a $\text{Ti}_3\text{C}_2\text{F}_{1.5}\text{O}_{0.5}$ surface or a $\text{Ti}_3\text{C}_2\text{F}_{0.5}\text{O}_{1.5}$ one. As evidenced in fig. 4, the calculated NMR shifts spread from the range of fully -F terminated surface to fully -O terminated surface in a monotonous way, with an approximately linear evolution. Focusing on the models corresponding to $\text{Ti}_3\text{C}_2\text{F}_{0.5}\text{O}_{1.5}$ surfaces (orange rectangle in fig. 4), one can see that the ^{13}C shift is not only sensitive to

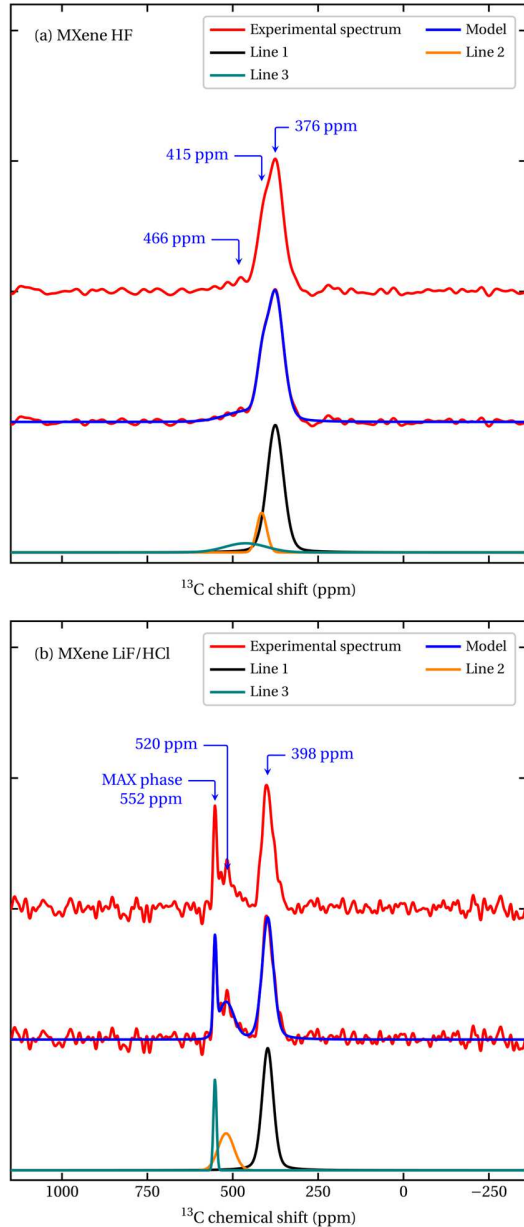


Figure 5. ^{13}C NMR spectra (red lines – top curves) recorded on $\text{Ti}_3\text{C}_2\text{T}_x$ samples etched with (a) HF and (b) LiF/HCl (see SI – part S1 for the synthesis protocols). The corresponding decomposition in terms of three gaussian functions in each case is given at the bottom and the global model (blue line) is superimposed to the experimental spectrum in the middle.

the composition of the closest surface but, for a given composition, it is also dependent on the atomic distribution of the first neighboring T-groups. This explains the drift regarding the linearity. Therefore, in the case of closely mixed -O and -F terminations homogeneously distributed on the MXene surface, we expect the ^{13}C NMR signal to be a single peak, the position of which would depend on the average O/F ratio. From the calculation point of view, we will consider in a first approximation that the effect of the mixing of surface terminations on the ^{13}C NMR shift can be evaluated

using the weighted average, based on the chemical composition, of the NMR shift values obtained from the model compounds (*i.e.* corresponding to a $\text{Ti}_3\text{C}_2\text{T}_2$ composition). A theoretical justification of this approximation is obtained by calculating the difference between the average of the NMR shifts obtained from the solid solution for each surface composition given in figure 4 (*i.e.* 25%F/75%O; 50%F/50%O and 25%F/75%O), and the corresponding value deduced from the model compounds (*e.g.* $0.25 \times \text{Ti}_3\text{C}_2\text{F}_2 + 0.75 \times \text{Ti}_3\text{C}_2\text{O}_2$ for a $\text{Ti}_3\text{C}_2\text{F}_{0.5}\text{O}_{1.5}$ composition). A mean error of 13 % is obtained which is similar to the average error expected from our correlation curve.

In order to validate our calculation protocol, comparisons were performed with the NMR shifts obtained experimentally for $\text{Ti}_3\text{C}_2\text{T}_x$ etched with the HF or LiF/HCl exfoliation processes (see SI part S1 for the synthesis protocols) presented in figure 5 a) and b), respectively. These spectra are in very good agreement with those reported by Hope *et al.*⁴⁰ The different contributions in these spectra, identified through the fitting of the experimental data using a minimum set of three gaussian functions in each case – labelled lines 1 to 3 –, are given at the bottom of the figure for each case. The global fit, which matches very well the experiment, is superimposed to the experimental data (middle curves in each case) and the details of the fits, *i.e.*, width, area, position of the gaussian functions, are given in SI – part S10. Focusing first on the HF sample, it is dominated by a broad asymmetric peak around 400 ppm which can be analyzed in terms of three contributions: a main one around 376 ppm (line 1) and two minor contributions around 415 and 466 ppm - labelled lines 2 and 3, respectively. Given our conclusions from the evolution of the ^{13}C NMR shift for solid solutions, the main peak at 376 ppm reflects a rather homogeneously distributed mixture of the surface groups rather than segregated O or F rich areas, which would result into two different contributions at higher and lower shift according to the values in table 3. Taking the XPS quantifications of Benchakar *et al.*²³ performed on $\text{Ti}_3\text{C}_2\text{T}_x$ flakes exfoliated with the very same protocol as that used for the samples investigated here, *i.e.* $\text{Ti}_3\text{C}_2.03\text{O}(\text{i})_{0.43}\text{O}(\text{ii})_{0.06}(\text{OH})_{0.30}\text{F}_{1.34}$, we obtain a value of $(0.49 \times 564 + 0.30 \times 339 + 1.34 \times 315) / (0.49 + 0.30 + 1.34) = 376$ ppm for the ^{13}C . This is in excellent agreement with the experimental value for the main peak.

Considering the two weaker contributions appearing at higher shifts, one can reasonably assume that they correspond to two other kinds of oxygen enriched regions. The one at highest shift, *i.e.* line 3, probably reflects very diverse local environments (both in terms of geometry and chemistry) for the corresponding carbon atoms as evidenced from the width of the corresponding signature which is significantly larger than that of lines 1 and 2. Considering an average NMR shift of 327 ppm for the -F and -(OH) groups (these two groups give very similar values as can be seen in table 3), one can estimate the average oxygen content y in these two regions from the corresponding ^{13}C experimental NMR shift values as follows (a global content of 2 T-group

per Ti_3C_2 formula was considered, as usually reported in the literature):

$$y = \frac{2 \cdot \delta_{\text{exp}} - 2 \cdot 327}{564 - 327} \quad (\text{eq. 6})$$

This gives oxygen contents of about 0.7 and 1.2 for the two regions, the highest oxygen content corresponding to the higher ^{13}C NMR shift. Beyond displaying an overall surface chemistry consistent with XPS quantifications as confirmed by the position of the main contribution of the ^{13}C signal, the HF-prepared MXene sheets thus also exhibit other oxygen enriched regions, the proportion of which can be estimated from the areas of the corresponding NMR peaks and correspond to 13 and 12 % of the global intensity for lines 2 and 3, respectively (for such estimates, the negligible effect of the T_2 relaxation time on the different contributions identified here has been checked, see SI part S11). These HF-prepared MXene layers exhibit non-uniform functionalization with oxygen-enriched regions, which is consistent with the fact that such a harsh environment favors the formation of defective layers^{23,68} leading to different local surface chemistries. In this regard, being able to identify the proportion of “damaged” MXene layers from NMR experiments is of great importance for the rationalization of MXene properties regarding the etching process.

Focusing now on the ^{13}C NMR spectrum collected on the LiF/HCl sample, given in figure 5 b, it appears to be significantly different from that of the HF sample. One can clearly distinguish three peaks at 552, 520 and 398 ppm. Hope *et al.* attributed the peaks at 552 and 520 ppm to Ti_3AlC_2 and TiC impurities, respectively.⁴⁰ Given that this MXene sample was synthesized from exactly the same batch of MAX phase powder as used for the HF samples, these results show that the MAX phase exfoliation is probably less effective using that etching agent. Compared to the HF sample, the MXene contribution appears at higher shift (*i.e.* 398 ppm vs 376 ppm) which is fully consistent with the higher oxygen content expected with this exfoliation protocol.²³ In addition, one can clearly notice that this contribution is fitted by a single component which, according to our previous analysis, reflects a much more homogeneous distribution of the surface groups on this MXene as compared to the HF-sample. This is consistent with the fact the LiF-HCl method leads to much less defective MXene layers as compared to the HF exfoliation process and thus to much more homogeneous environment. Taking the XPS composition for these MXene layers, *i.e.* $\text{Ti}_3\text{C}_{1.94}\text{O}(\text{i})_{0.71}\text{O}(\text{ii})_{0.23}(\text{OH})_{0.17}\text{F}_{0.75}$,²³ we get a theoretical ^{13}C NMR shift of around 443 ppm which is higher than the 398 ppm experimental value, but is still satisfactory considering our uncertainty. However, it is very interesting to notice that the 443 ppm value is very close to an average between the 520 and 398 ppm experimental peaks. Given the very similar broadening of lines 1 and 2 (see SI – part S10), which is significantly larger than that corresponding to the well crystallized Ti_3AlC_2 phase, and the fact that the average value between the 520 and 398 ppm shifts (*i.e.* 459 ppm) is very close to NMR shift deduced from the XPS composition of the flakes, one could also attribute this broad 520 ppm peak to another MXene contribution, and not to TiC as proposed previously. Such an interpretation would underline two kinds of segregated regions in terms of surface functionalization, with partially F-rich or O-rich

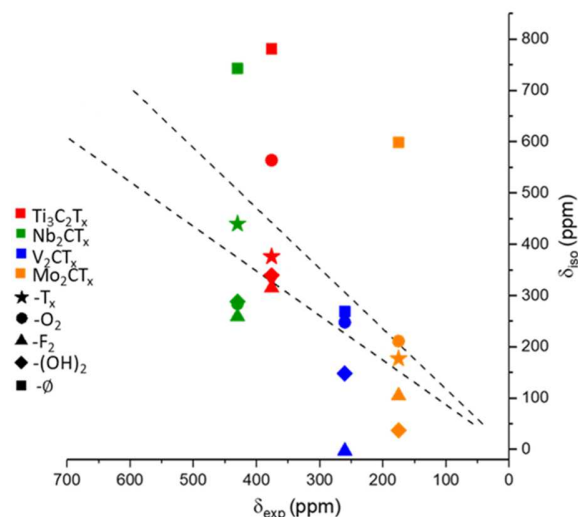


Figure 6. Correlation between the calculated (y-axis) and experimental (x-axis) ^{13}C NMR shifts in different MXenes synthesized using the HF exfoliation process: $\text{Ti}_3\text{C}_2\text{T}_x$ (red), Nb_2CT_x (green), V_2CT_x (blue) and Mo_2CT_x (orange). Dashed lines represent the uncertainty of our theoretical model, *i.e.* $\pm 15\%$. MXenes’ NMR experimental and calculated shifts are plotted for different surface terminations: no termination (square), -O (circle), -F (triangle up), -(OH) (diamond) and - T_x average theoretical calculated NMR shifts deduced from the XPS quantifications of references 23, 28 and 69 (star).

regions. Using the same approach as for the HF sample one obtains O contents of 1.7 for line 2 (with a relative amount of 24 % of the global intensity) and 0.6 for line 1 (with a relative amount of 64 %). The negligible effect of the T_2 relaxation time on these signals has again been checked (see SI part S11). Such a hypothesis, which will have to be confirmed by other characterizations, would give new perspectives on the role of the exfoliation process on the MXene surface by highlighting an effect on the average content of the different T-groups, but also on their spatial distribution.

Given the possibility that it offers in probing large volumes, ^{13}C NMR thus appears as a very interesting tool allowing to extend the analysis of the surface chemistry of $\text{Ti}_3\text{C}_2\text{T}_x$ MXene sheets beyond what is usually obtained with other local probes techniques such as XPS or TEM-based spectroscopies, which intrinsically probe smaller volumes. In addition, given its very high sensitivity to local environment changes around the C atoms, ^{13}C NMR shifts also give access to important characteristics of the $\text{Ti}_3\text{C}_2\text{T}_x$ sheets such as the number of composition variants, their relative amount and dispersion in terms of structural disorder. Considering the crucial role played by oxygen groups on Ti-based MXenes (*e.g.*, possible band gap opening⁵⁵ or improvement on energy storage capacity⁶⁹), such information is key to the rationalization and optimization of their properties in many application fields. The information provided at the ^{13}C NMR signal can also be correlated to the density of defects in the MXenes layers, providing a rather complete description of the layer’s functionalization.

Extension to other MXenes. Following the results obtained on the benchmark $\text{Ti}_3\text{C}_2\text{T}_x$ MXene, we end by proposing an analysis of the sensitivity of the ^{13}C NMR shift on their

functionalization for other systems investigated in the literature, *i.e.* V_2CT_x ,³⁹ Nb_2CT_x ,⁴² and Mo_2CT_x ,⁴⁹ and having different M-elements. A quantitative analysis like that provided for $Ti_3C_2T_x$ is however more difficult to elaborate since the compositions of the different MXenes are generally not given in the corresponding references excepted for V_2CT_x where Harris *et al.* proposed $V_2CF(OH)$.³⁹ We will therefore first focus this discussion on the computational aspect. With that respect, it is important to notice that we here stick to the GGA level for our DFT simulations: this approximation is expected to be rather good for Nb_2CT_x and Mo_2CO_2 ⁵⁶ but could not give the right ground state for V_2C . The results obtained for the ^{13}C NMR shifts for four different terminations, *i.e.* =O, -(OH), -F and pristine surfaces, are summarized in figure 6. The NMR shifts for -Cl surface terminations were not investigated as all these materials were synthesized using the HF approach, avoiding the presence of chlorine as terminal groups. Figure 6 plots the calculated NMR shifts, based on equation 5, versus the experimental δ_{exp} NMR shifts in the studied MXenes. Colors stand for a given MXene: $Ti_3C_2T_2$ (red), Nb_2CT_2 (green), V_2CT_2 (blue) and Mo_2CT_2 (orange) and the symbols differentiate the type of surface terminations: -O (circle), -F (triangle up), -(OH) (diamond), and bare MXenes (square). The dashed lines represent the 15% uncertainty estimated for our simulations. The corresponding numerical data are given in table S12 in the supporting information. The data discussed previously on the HF $Ti_3C_2T_x$ sample are also given.

One first notices from these calculations that the pristine surfaces generally induce a very significant ^{13}C shift to higher values compared of the functionalized surfaces. This points ^{13}C NMR as a very sensitive probe for surface vacancies. Another important conclusion that can be drawn from our data is that, depending on the nature of M, the different surface terminations do not induce the same shift of the ^{13}C NMR signal. For example, for the Nb_2CT_x MXene, the different surface groups give almost the same value for the ^{13}C shift, ranging from 259 ppm for Nb_2CF_2 to 288ppm for $Nb_2C(OH)_2$. This is in striking difference with $Ti_3C_2T_2$ systems for instance. For this particular case and disregarding potential defects in the MXene layer due to, *e.g.* the exfoliation step, the ^{13}C NMR signal is thus expected to be mainly influenced by the amount of vacancies on the MXene surface. Considering the Mo_2CT_x system, functional groups do affect the NMR chemical shift with -(OH) groups giving the lowest NMR shift (~ 37 ppm) and oxygen-terminated layers the largest one (~ 211 ppm). It is noticeable from table S12, that these changes are mainly due to the spin component of the shielding, pointing out the crucial role of the terminations on the electron population at the Fermi level.

Although no surface chemistry is available for the Nb_2CT_x and Mo_2CT_x MXenes investigated by NMR^{42,49}, one can think of taking compositions determined in other studies to compare our calculations with the experimental data. For the present purpose and to be consistent with the approach developed for $Ti_3C_2T_x$, we used the XPS quantifications of Halim *et al.* for the Nb_2CT_x and Mo_2CT_x systems, both being performed on concentrated HF-exfoliated MXenes like the samples investigated by NMR.^{28,69} We however expect such an approach to have a rather limited applicability since MXenes surface chemistry and quality is known to critically depend on the MAX phase precursors^{23,70} as well as on the

details of the etching process (*e.g.*, duration of exfoliation, temperature, delamination conditions, drying step)²³ which usually differ from one study to another. Focusing on Nb_2CT_x two XPS compositions were proposed by J. Halim *et al.*,²⁸ obtained before and after surface sputtering and corresponding respectively to: $Nb_2CO_{0.8}(OH,H_2O_{ads})_{0.5}F_{0.7}$ and $Nb_2CO_{0.9}O_{0.6}(OH)_{0.01}(OH,H_2O_{ads})_{0.3}F_{0.4}$. Assuming that the OH and OH, H_2O_{ads} contributions can be both described by the $Nb_2C(OH)_2$ system and adding a 2-x contribution of the pristine surface when $x < 2$, we predict the following NMR shifts for these two compositions: 276 ppm and 438 ppm (green star in fig.6), respectively. Compared to the experimental value, *i.e.* 430 ppm, the composition obtained by XPS after sputtering leads to a quite remarkable agreement. Similarly, the XPS composition of reference 69 by J. Halim *et al.*⁶⁹ for the Mo-based system, *i.e.* $Mo_2CO_{0.6}(OH)_{0.4}(OH,H_2O)_{0.6}F_{0.1}$, leads to a theoretical NMR shift of 177 ppm (orange star in fig.6), which is very close to the experimental value reported by Deeva *et al.*, 175 ppm.⁴⁹ Although such good agreements were quite unexpected given the limitations mentioned before, it gives strong support to the calculations presented in this study. Our calculated values for Nb_2CT_x and Mo_2CT_x can thus probably be used to analyze the ^{13}C NMR shift in these materials provided the adequate characterization of their surface chemistry is performed. This highlights the potentially large appeal of the here-proposed method, based on the comparison between experiments and simulations of the ^{13}C NMR signal, for the rationalization of the surface functionalization of MXene sheets.

CONCLUSIONS

As a summary, a comparative study of experimental ^{13}C NMR shifts and corresponding simulated shielding from first-principles calculations in MAX phases and MXenes has been provided. Calculations were performed considering both the orbital and spin contributions to the magnetic shielding, a complete scheme which proved to be essential to fully describe the investigated materials. A methodology for the interpretation of the calculated magnetic shielding was developed considering a set of eleven reference materials, including MAX phases, Mo_2Ga_2C and TiC, with different structures and chemical compositions. The importance of considering the spin contribution to the shielding (Knight Shift) in the total magnetic shielding is clearly emphasized as it may be the dominant component for some compositions and varies significantly from one MAX phase to another, all MAX phases being metallic. Based on the analysis performed on MAX phases, a linear relationship allowing to directly connect the isotropic calculated ^{13}C NMR shielding δ_{iso} to the experimental value δ_{exp} has been obtained and was shown to give very good results.

The developed methodology has then been used to assess the role of the surface functionalization on the ^{13}C NMR spectra in the $Ti_3C_2T_x$, Nb_2CT_x , V_2CT_x and Mo_2CT_x MXenes. Using $Ti_3C_2T_x$ as a benchmark MXene, we assessed the influence of different structural parameters related to the surface groups (*e.g.* their position or their mixing on the MXene surface) on the ^{13}C NMR shifts. We could thus propose a very simple approach allowing to take these parameters into account based on the weighted average of NMR shifts calculated in model systems. Based on this methodology, we show that the ^{13}C NMR shifts can be related to the surface

chemistry of the $Ti_3C_2T_x$ MXene sheets in a quantitative way and, beyond that, allows to identify and quantify different composition variants in a single batch which is hardly possible with other more local techniques. In addition, we propose that the choice of the etching agent may not only influence the nature of the surface groups but their spatial distribution onto the surface too. Our theoretical protocol has been extended to three other MXenes showing very diverse effects of the surface groups on the calculated ^{13}C NMR shifts and overall good agreement with experimental data from the literature.

As a conclusion, we show that first-principles calculations of the NMR shielding in MXenes can be used as a predictive tool and quantitative support for the interpretation of ^{13}C NMR spectra in this very large class of 2D materials. This signature offers direct information on the nature of the surface termination in $Ti_3C_2T_x$ (and most probably on other MXenes), as well as their spatial distribution and number of compositional variants. Given the crucial role played by the functionalization on their properties and the numerous opportunities provided by NMR to dynamically probe materials behavior under operating conditions, combining DFT simulations with NMR experiments - especially for ^{13}C - opens large opportunities to better characterize and understand MXene materials for future applications.

ASSOCIATED CONTENT

Supporting Information.

This material is available free of charge via the Internet at <http://pubs.acs.org>.

MAX phases and MXene synthesis; Structural models corresponding to the $M_{n+1}X_nO_2$ systems; Structural parameters for the calculations; PAW potentials and k-points convergence of the NMR shielding; Comparison between GGA and exact exchange calculations; Comparison between scalar relativistic and fully relativistic calculations; ^{13}C NMR spectra of Ti_2AlC , Mo_2TiAlC_2 , $Mo_2Ti_2AlC_2$ and Mo_2Ga_2C ; Numerical values of the orbital, contact and dipolar contributions to the ^{13}C NMR shielding in MAX phases; Structural models corresponding to the $Ti_3C_2(O_{3/4},F_{1/4})_2$ and $Ti_3C_2(O_{1/2},F_{1/2})_2$ solid solutions discussed in figure 4; Fits of the experimental ^{13}C NMR spectra of the HF and LiF-HCl prepared $Ti_3C_2T_x$ samples; Effect of the T_2 relaxation time on the NMR spectra in $Ti_3C_2T_x$; Numerical values of the orbital, contact and dipolar contributions to the ^{13}C NMR shielding in MXenes with different surface terminations.

AUTHOR INFORMATION

Corresponding Authors

Vincent Mauchamp – *Department of Physical and Mechanical Properties of Materials – Université de Poitiers, ISAE-ENSMA, CNRS, PPRIME, Poitiers, France*

Email : vincent.mauchamp@univ-poitiers.fr

Florent Boucher – *Nantes Université, CNRS, Institut des Matériaux de Nantes Jean Rouxel, IMN, F-44000 Nantes, France*

Email : Florent.Boucher@cnrs-imn.fr

Authors

Florian Brette – *Department of Physical and Mechanical Properties of Materials – Université de Poitiers, ISAE-ENSMA, CNRS, PPRIME, Poitiers, France & Nantes Université, CNRS, Institut des Matériaux de Nantes Jean Rouxel, IMN, F-44000 Nantes, France*

Dani Kourati – *CNRS, CEMHTI UPR3079, Université d'Orléans, Orléans, France*

Michael Paris – *Nantes Université, CNRS, Institut des Matériaux de Nantes Jean Rouxel, IMN, F-44000 Nantes, France*

Lola Loupias – *Institut de Chimie des Milieux et Matériaux de Poitiers (IC2MP), Université de Poitiers, CNRS, F-86073 Poitiers, France*

Stéphane Célérier – *Institut de Chimie des Milieux et Matériaux de Poitiers (IC2MP), Université de Poitiers, CNRS, F-86073 Poitiers, France*

Thierry Cabioch – *Department of Physical and Mechanical Properties of Materials – Université de Poitiers, ISAE-ENSMA, CNRS, PPRIME, Poitiers, France*

Michael Deschamps – *CNRS, CEMHTI UPR3079, Université d'Orléans, Orléans, France*

Funding Sources

Agence National de la Recherche: reference ANR-18-CE08-014 – MXENECAT project

French government program 'Investissements d'Avenir': EUR INTREE, Reference ANR-18-EURE-0010

ACKNOWLEDGMENT

The authors acknowledge financial support from the "Agence National de la Recherche" (reference ANR-18-CE08-014 – MXENECAT project). The PhD thesis of F. Brette and L. Loupias were funded by the MXENECAT project (reference ANR-18-CE08-014). This work was supported by the French government program 'Investissements d'Avenir' (EUR INTREE, Reference ANR-18-EURE-0010). The authors acknowledge financial support from the European Union (ERDF) and Région Nouvelle Aquitaine. A. Habrioux and C. Morais (IC2MP) are here thanked for the fruitful discussions around the present results. P. Chartier is gratefully acknowledged for assistance in the synthesis of Mo_2Ga_2C .

REFERENCES

- (1) Novoselov, K. S.; Geim, A. K.; Morozov, S. V.; Jiang, D.; Zhang, Y.; Dubonos, S. V.; Grigorieva, I. V.; Firsov, A. A. Electric Field Effect in Atomically Thin Carbon Films. *Science* **2004**, *306* (5696), 666–669.
- (2) VahidMohammadi, A.; Rosen, J.; Gogotsi, Y. The World of Two-Dimensional Carbides and Nitrides (MXenes). *Science* **2021**, *372* (6547), eabf1581.
- (3) Naguib, M.; Barsoum, M. W.; Gogotsi, Y. Ten Years of Progress in the Synthesis and Development of MXenes. *Adv. Mater.* **2021**, *33* (39), 2103393.
- (4) Barsoum, M. W. *MAX Phases: Properties of Machinable Ternary Carbides and Nitrides*; Wiley-VCH; 2013.
- (5) Sokol, M.; Natu, V.; Kota, S.; Barsoum, M. W. On the Chemical Diversity of the MAX Phases. *Trends Chem.* **2019**, *1* (2), 210–223.
- (6) Anasori, B.; Shi, C.; Moon, E. J.; Xie, Y.; Voigt, C. A.; Kent, P. R. C.; May, S. J.; Billinge, S. J. L.; Barsoum, M. W.; Gogotsi, Y. Control of Electronic Properties of 2D Carbides (MXenes) by Manipulating

- Their Transition Metal Layers. *Nanoscale Horiz.* **2016**, *1* (3), 227–234.
- (7) Naguib, M.; Kurtoglu, M.; Presser, V.; Lu, J.; Niu, J.; Heon, M.; Hultman, L.; Gogotsi, Y.; Barsoum, M. W. Two-Dimensional Nanocrystals Produced by Exfoliation of Ti_3AlC_2 . *Adv. Mater.* **2011**, *23* (37), 4248–4253.
- (8) Gogotsi, Y.; Anasori, B. The Rise of MXenes. *ACS Nano* **2019**, *13* (8), 8491–8494.
- (9) Ghidui, M.; Lukatskaya, M. R.; Zhao, M.-Q.; Gogotsi, Y.; Barsoum, M. W. Conductive Two-Dimensional Titanium Carbide ‘Clay’ with High Volumetric Capacitance. *Nature* **2014**, *516* (7529), 78–81.
- (10) Anasori, B.; Lukatskaya, M. R.; Gogotsi, Y. 2D Metal Carbides and Nitrides (MXenes) for Energy Storage. *Nat. Rev. Mater.* **2017**, *2* (2), 16098.
- (11) Shahzad, F.; Alhabeab, M.; Hatter, C. B.; Anasori, B.; Man Hong, S.; Koo, C. M.; Gogotsi, Y. Electromagnetic Interference Shielding with 2D Transition Metal Carbides (MXenes). *Science* **2016**, *353* (6304), 1137–1140.
- (12) Pei, Y.; Zhang, X.; Hui, Z.; Zhou, J.; Huang, X.; Sun, G.; Huang, W. $Ti_3C_2T_x$ MXene for Sensing Applications: Recent Progress, Design Principles, and Future Perspectives. *ACS Nano* **2021**, *15* (3), 3996–4017.
- (13) Zhang, C. (John); Nicolosi, V. Graphene and MXene-Based Transparent Conductive Electrodes and Supercapacitors. *Energy Storage Mater.* **2019**, *16*, 102–125.
- (14) Huang, L.; Ding, L.; Haihui, W. MXene-Based Membranes for Separation Applications. *Small Sci* **2021**, *1* (7), 2100013.
- (15) Hu, T.; Hu, M.; Li, Z.; Zhang, H.; Zhang, C.; Wang, J.; Wang, X. Interlayer Coupling in Two-Dimensional Titanium Carbide MXenes. *Phys. Chem. Chem. Phys.* **2016**, *18* (30), 20256–20260.
- (16) Khakbaz, P.; Moshayedi, M.; Hajian, S.; Soleimani, M.; Narakathu, B. B.; Bazuin, B. J.; Pourfath, M.; Atashbar, M. Z. Titanium Carbide MXene as NH_3 Sensor: Realistic First-Principles Study. *J. Phys. Chem. C* **2019**, *123* (49), 29794–29803.
- (17) Lee, E.; VahidMohammadi, A.; Prorok, B. C.; Yoon, Y. S.; Beidaghi, M.; Kim, D.-J. Room Temperature Gas Sensing of Two-Dimensional Titanium Carbide (MXene). *ACS Appl. Mater. Interfaces* **2017**, *9* (42), 37184–37190.
- (18) Chen, W. Y.; Lai, S.-N.; Yen, C.-C.; Jiang, X.; Peroulis, D.; Stanciu, L. A. Surface Functionalization of $Ti_3C_2T_x$ MXene with Highly Reliable Superhydrophobic Protection for Volatile Organic Compounds Sensing. *ACS Nano* **2020**, *14* (9), 11490–11501.
- (19) Malchik, F.; Shpigel, N.; Levi, M. D.; Penki, T. R.; Gavriel, B.; Bergman, G.; Turgeman, M.; Aurbach, D.; Gogotsi, Y. MXene Conductive Binder for Improving Performance of Sodium-Ion Anodes in Water-in-Salt Electrolyte. *Nano Energy* **2021**, *79*, 105433.
- (20) Hantanasirisakul, K.; Gogotsi, Y. Electronic and Optical Properties of 2D Transition Metal Carbides and Nitrides (MXenes). *Adv. Mater.* **2018**, *30* (52), 1804779.
- (21) Kamysbayev, V.; Filatov, A. S.; Hu, H.; Rui, X.; Lagunas, F.; Wang, D.; Klie, R. F.; Talapin, D. V. Covalent Surface Modifications and Superconductivity of Two-Dimensional Metal Carbide MXenes. *Science* **2020**, *369* (6506), 979–983.
- (22) Frey, N. C.; Bandyopadhyay, A.; Kumar, H.; Anasori, B.; Gogotsi, Y.; Shenoy, V. B. Surface-Engineered MXenes: Electric Field Control of Magnetism and Enhanced Magnetic Anisotropy. *ACS Nano* **2019**, *13* (3), 2831–2839.
- (23) Benchakar, M.; Loupias, L.; Garnero, C.; Bilyk, T.; Morais, C.; Canaff, C.; Guignard, N.; Morisset, S.; Pazniak, H.; Hurand, S.; Paccard, J.; Mauchamp, V.; Barsoum, M. W.; Habrioux, A.; Célérier, S. One MAX Phase, Different MXenes: A Guideline to Understand the Crucial Role of Etching Conditions on $Ti_3C_2T_x$ Surface Properties. *Appl. Surf. Sci.* **2020**, *530*, 147209.
- (24) Natu, V.; Benchakar, M.; Canaff, C.; Habrioux, A.; Célérier, S.; Barsoum, M. W. A Critical Analysis of the X-Ray Photoelectron Spectra of $Ti_3C_2T_x$ MXenes. *Matter* **2021**, S2590238521000151.
- (25) Persson, I.; Näslund, L.-Åke; Halim, J.; Barsoum, M. W.; Darakchieva, V.; Palisaitis, J.; Rosen, J.; Persson, P. O. Å. On the Organization and Thermal Behavior of Functional Groups on Ti_3C_2 MXene Surfaces in Vacuum. *2D Mater.* **2017**, *5* (1), 015002.
- (26) Persson, I.; Halim, J.; Lind, H.; Hansen, T. W.; Wagner, J. B.; Näslund, L.-Å.; Darakchieva, V.; Palisaitis, J.; Rosen, J.; Persson, P. O. Å. 2D Transition Metal Carbides (MXenes) for Carbon Capture. *Adv. Mater.* **2019**, *31* (2), 1805472.
- (27) Gogotsi, Y.; Huang, Q. MXenes: Two-Dimensional Building Blocks for Future Materials and Devices. *ACS Nano* **2021**, *15* (4), 5775–5780.
- (28) Halim, J.; Cook, K. M.; Naguib, M.; Eklund, P.; Gogotsi, Y.; Rosen, J.; Barsoum, M. W. X-Ray Photoelectron Spectroscopy of Select Multi-Layered Transition Metal Carbides (MXenes). *Appl. Surf. Sci.* **2016**, *362*, 406–417.
- (29) Wang, X.; Shen, X.; Gao, Y.; Wang, Z.; Yu, R.; Chen, L. Atomic-Scale Recognition of Surface Structure and Intercalation Mechanism of $Ti_3C_2T_x$. *J. Am. Chem. Soc.* **2015**, *137* (7), 2715–2721.
- (30) Magne, D.; Mauchamp, V.; Célérier, S.; Chartier, P.; Cabioch, T. Site-Projected Electronic Structure of Two-Dimensional Ti_3C_2 MXene: The Role of the Surface Functionalization Groups. *Phys. Chem. Chem. Phys.* **2016**, *18* (45), 30946–30953.
- (31) Karlsson, L. H.; Birch, J.; Halim, J.; Barsoum, M. W.; Persson, P. O. Å. Atomically Resolved Structural and Chemical Investigation of Single MXene Sheets. *Nano Lett* **2015**, *15* (8), 4955–4960.
- (32) Magne, D.; Mauchamp, V.; Célérier, S.; Chartier, P.; Cabioch, T. Spectroscopic Evidence in the Visible-Ultraviolet Energy Range of Surface Functionalization Sites in the Multilayer Ti_3C_2 MXene. *Phys. Rev. B* **2015**, *91* (20), 201409.
- (33) Wang, H.-W.; Naguib, M.; Page, K.; Wesolowski, D. J.; Gogotsi, Y. Resolving the Structure of $Ti_3C_2T_x$ MXenes through Multilevel Structural Modeling of the Atomic Pair Distribution Function. *Chem. Mater.* **2016**, *28* (1), 349–359.
- (34) Hu, T.; Wang, J.; Zhang, H.; Li, Z.; Hu, M.; Wang, X. Vibrational Properties of Ti_3C_2 and $Ti_3C_2T_2$ (T = O, F, OH) Monosheets by First-Principles Calculations: A Comparative Study. *Phys Chem Chem Phys* **2015**, *17*, 9997.
- (35) Sarycheva, A.; Gogotsi, Y. Raman Spectroscopy Analysis of the Structure and Surface Chemistry of $Ti_3C_2T_x$ MXene. *Chem. Mater.* **2020**, *32* (8), 3480–3488.
- (36) Dorn, R. W.; Ryan, M. J.; Kim, T.-H.; Goh, T. W.; Venkatesh, A.; Heintz, P. M.; Zhou, L.; Huang, W.; Rossini, A. J. Identifying the Molecular Edge Termination of Exfoliated Hexagonal Boron Nitride Nanosheets with Solid-State NMR Spectroscopy and Plane-Wave DFT Calculations. *Chem. Mater.* **2020**, *32* (7), 3109–3121.
- (37) Wild, S.; Dinh, X. T.; Maid, H.; Hauke, F.; Abellán, G.; Hirsch, A. Quantifying the Covalent Functionalization of Black Phosphorus. *Angew. Chem. Int. Ed.* **2020**, *59* (45), 20230–20234.
- (38) Rawal, A.; Che Man, S. H.; Agarwal, V.; Yao, Y.; Thickett, S. C.; Zetterlund, P. B. Structural Complexity of Graphene Oxide: The Kirigami Model. *ACS Appl. Mater. Interfaces* **2021**, *13* (15), 18255–18263.
- (39) Harris, K. J.; Bugnet, M.; Naguib, M.; Barsoum, M. W.; Goward, G. R. Direct Measurement of Surface Termination Groups and Their Connectivity in the 2D MXene V_2CT_x Using NMR Spectroscopy. *J. Phys. Chem. C* **2015**, *119* (24), 13713–13720.
- (40) Hope, M. A.; Forse, A. C.; Griffith, K. J.; Lukatskaya, M. R.; Ghidui, M.; Gogotsi, Y.; Grey, C. P. NMR Reveals the Surface Functionalisation of Ti_3C_2 MXene. *Phys. Chem. Chem. Phys.* **2016**, *18* (7), 5099–5102.

- (41) Anayee, M.; Kurra, N.; Alhabeab, M.; Seredych, M.; Hedhili, M. N.; Emwas, A.-H.; Alshareef, H. N.; Anasori, B.; Gogotsi, Y. Role of Acid Mixtures Etching on the Surface Chemistry and Sodium Ion Storage in $Ti_3C_2T_x$ MXene. *Chem. Commun.* **2020**, *56* (45), 6090–6093.
- (42) Griffith, K. J.; Hope, M. A.; Reeves, P. J.; Anayee, M.; Gogotsi, Y.; Grey, C. P. Bulk and Surface Chemistry of the Niobium MAX and MXene Phases from Multinuclear Solid-State NMR Spectroscopy. *J. Am. Chem. Soc.* **2020**, *142* (44), 18924–18935.
- (43) Kobayashi, T.; Sun, Y.; Prenger, K.; Jiang, D.; Naguib, M.; Pruski, M. Nature of Terminating Hydroxyl Groups and Intercalating Water in $Ti_3C_2T_x$ MXenes: A Study by 1H Solid-State NMR and DFT Calculations. *J. Phys. Chem. C* **2020**, *124* (25), 13649–13655.
- (44) Mauri, F.; Pfrommer, B. G.; Louie, S. G. *Ab Initio* Theory of NMR Chemical Shifts in Solids and Liquids. *Phys. Rev. Lett.* **1996**, *77* (26), 5300–5303.
- (45) Pickard, C. J.; Mauri, F. All-Electron Magnetic Response with Pseudopotentials: NMR Chemical Shifts. *Phys. Rev. B* **2001**, *63* (24), 245101.
- (46) Laskowski, R.; Blaha, P. NMR Shielding in Metals Using the Augmented Plane Wave Method. *J. Phys. Chem. C* **2015**, *119* (33), 19390–19396.
- (47) Laskowski, R.; Khoo, K. H.; Haarmann, F.; Blaha, P. Computational Study of Ga NMR Shielding in Metallic Gallides. *J. Phys. Chem. C* **2017**, *121* (1), 753–760.
- (48) Khoo, K. H.; Laskowski, R.; Blaha, P. Computational Study of Al and Sc NMR Shielding in Metallic ScTT'Al Heusler Phases. *J. Phys. Chem. C* **2017**, *121* (22), 12398–12406.
- (49) Deeva, E. B.; Kurlov, A.; Abdala, P. M.; Lebedev, D.; Kim, S. M.; Gordon, C. P.; Tsoukalou, A.; Fedorov, A.; Müller, C. R. In Situ XANES/XRD Study of the Structural Stability of Two-Dimensional Molybdenum Carbide Mo_2CT_x : Implications for the Catalytic Activity in the Water–Gas Shift Reaction. *Chem. Mater.* **2019**, *31* (12), 4505–4513.
- (50) Sun, W.; Wang, H.; Vlcek, L.; Peng, J.; Brady, A. B.; Osti, N. C.; Mamontov, E.; Tyagi, M.; Nanda, J.; Greenbaum, S. G.; Kent, P. R. C.; Naguib, M. Multiscale and Multimodal Characterization of 2D Titanium Carbonitride MXene. *Adv. Mater. Interfaces* **2020**, *7* (11), 1902207.
- (51) Kajiyama, S.; Szabova, L.; Sodeyama, K.; Iinuma, H.; Morita, R.; Gotoh, K.; Tateyama, Y.; Okubo, M.; Yamada, A. Sodium-Ion Intercalation Mechanism in MXene Nanosheets. *ACS Nano* **2016**, *10* (3), 3334–3341.
- (52) Maughan, P. A.; Bouscarrat, L.; Seymour, V. R.; Shao, S.; Haigh, S. J.; Dawson, R.; Tapia-Ruiz, N.; Bimbo, N. Pillared Mo_2TiC_2 MXene for High-Power and Long-Life Lithium and Sodium-Ion Batteries. *Nanoscale Adv.* **2021**, *3* (11), 3145–3158.
- (53) Schultz, T.; Frey, N. C.; Hantanasirisakul, K.; Park, S.; May, S. J.; Shenoy, V. B.; Gogotsi, Y.; Koch, N. Surface Termination Dependent Work Function and Electronic Properties of $Ti_3C_2T_x$ MXene. *Chem. Mater.* **2019**, *31* (17), 6590–6597.
- (54) Momma, K.; Izumi, F. VESTA3 for Threedimensional Visualization of Crystal, Volumetric and Morphology Data. *J. Appl. Cryst.* **2011**, *44*, 1272.
- (55) Khazaei, M.; Arai, M.; Sasaki, T.; Chung, C.-Y.; Venkataramanan, N. S.; Estili, M.; Sakka, Y.; Kawazoe, Y. Novel Electronic and Magnetic Properties of TwoDimensional Transition Metal Carbides and Nitrides. *Adv. Funct. Mater.* **2013**, *23* (7), 2185–2192.
- (56) Bae, S.; Kang, Y.-G.; Khazaei, M.; Ohno, K.; Kim, Y.-H.; Han, M. J.; Chang, K. J.; Raebiger, H. Electronic and Magnetic Properties of Carbide MXenes—the Role of Electron Correlations. *Mater. Today Adv.* **2021**, *9*, 100118.
- (57) Blaha, P.; Schwarz, K.; Madsen, G. K. H.; Kvasnicka, D.; Luitz, J.; Laskowski, R.; Tran, F.; Marks, L. D. An Augmented Plane Wave + Local Orbitals Program for Calculating Crystal Properties. **2019**, 287.
- (58) Blaha, P.; Schwarz, K.; Tran, F.; Laskowski, R.; Madsen, G. K. H.; Marks, L. D. WIEN2k: An APW+lo Program for Calculating the Properties of Solids. *J. Chem. Phys.* **2020**, *152* (7), 074101.
- (59) Kresse, G.; Furthmüller, J. Efficient Iterative Schemes for *Ab Initio* Total-Energy Calculations Using a Plane-Wave Basis Set. *Phys. Rev. B* **1996**, *54* (16), 18.
- (60) Kresse, G.; Joubert, D. From Ultrasoft Pseudopotentials to the Projector Augmented-Wave Method. *Phys. Rev. B* **1999**, *59* (3), 18.
- (61) Yates, J. R.; Pickard, C. J.; Mauri, F. Calculation of NMR Chemical Shifts for Extended Systems Using Ultrasoft Pseudopotentials. *Phys. Rev. B* **2007**, *76* (2), 024401.
- (62) Blügel, S.; Akai, H.; Zeller, R.; Dederichs, P. H. Hyperfine Fields of 3 *d* and 4 *d* Impurities in Nickel. *Phys. Rev. B* **1987**, *35* (7), 3271–3283.
- (63) Perdew, J. P.; Burke, K.; Ernzerhof, M. Generalized Gradient Approximation Made Simple. *Phys. Rev. Lett.* **1996**, *77* (18), 3865–3868.
- (65) Monkhorst, H. J.; Pack, J. D. Special Points for Brillouin-Zone Integrations. *Phys. Rev. B* **1976**, *13* (12), 5188–5192.
- (65) Siegel, R.; Nakashima, T. T.; Wasylishen, R. E. Signal-to-Noise Enhancement of NMR Spectra of Solids Using Multiple-Pulse Spin-Echo Experiments. *Concepts Magn. Reson. Part A* **2005**, *26A* (2), 62–77.
- (66) Massiot, D.; Fayon, F.; Capron, M.; King, I.; Le Calvé, S.; Alonso, B.; Durand, J.-O.; Bujoli, B.; Gan, Z.; Hoatson, G. Modelling One- and Two-Dimensional Solid-State NMR Spectra. *Magn. Reson. Chem.* **2002**, *40* (1), 70–76.
- (67) Sang, X.; Xie, Y.; Lin, M.-W.; Alhabeab, M.; Van Aken, K. L.; Gogotsi, Y.; Kent, P. R. C.; Xiao, K.; Unocic, R. R. Atomic Defects in Monolayer Titanium Carbide ($Ti_3C_2T_x$) MXene. *ACS Nano* **2016**, *10* (10), 9193–9200.
- (68) Xie, Y.; Naguib, M.; Mochalin, V. N.; Barsoum, M. W.; Gogotsi, Y.; Yu, X.; Nam, K.-W.; Yang, X.-Q.; Kolesnikov, A. I.; Kent, P. R. C. Role of Surface Structure on Li-Ion Energy Storage Capacity of Two-Dimensional Transition-Metal Carbides. *J. Am. Chem. Soc.* **2014**, *136* (17), 6385–6394.
- (69) Halim, J.; Kota, S.; Lukatskaya, M. R.; Naguib, M.; Zhao, M.-Q.; Moon, E. J.; Pitock, J.; Nanda, J.; May, S. J.; Gogotsi, Y.; Barsoum, M. W. Synthesis and Characterization of 2D Molybdenum Carbide (MXene). *Adv. Funct. Mater.* **2016**, *26* (18), 3118–3127.
- (70) Shuck, C. E.; Han, M.; Maleski, K.; Hantanasirisakul, K.; Kim, S. J.; Choi, J.; Reil, W. E. B.; Gogotsi, Y. Effect of Ti_3AlC_2 MAX Phase on Structure and Properties of Resultant $Ti_3C_2T_x$ MXene. *ACS Appl. Nano Mater.* **2019**, *2* (6), 3368–3376.